Rational conversion of chromophore selectivity of cyanobacteriochromes to accept mammalian intrinsic biliverdin

メタデータ	言語: English 出版者: PNAS 公開日: 2019-06-07 キーワード (Ja): キーワード (En): bilin, in vivo imaging, protein engineering 作成者: Fushimi, Keiji, Miyazaki, Takatsugu, Kuwasaki, Yuto, Nakajima, Takahiro, Yamamoto, Tatsuro, Suzuki, Kazushi, Ueda, Yoshibumi, Miyake, Keita, Takeda, Yuka, Choi, Jae-Hoon, Kawagishi, Hirokazu, Park, Enoch Y., Ikeuchi, Masahiko, Sato, Moritoshi, Narikawa, Rei メールアドレス: 所属:
URL	http://hdl.handle.net/10297/00026661

Rational conversion of chromophore selectivity of cyanobacteriochromes to accept mammalian intrinsic biliverdin

Keiji Fushimi[*,†], Takatsugu Miyazaki[*,‡], Yuto Kuwasaki[§], Takahiro Nakajima[§], Tatsuro Yamamoto[*], Kazushi Suzuki[§], Yoshibumi Ueda[§,¶], Keita Miyake[*], Yuka Takeda[*], Jae-Hoon Choi[*,‡], Hirokazu Kawagishi[*,‡], Enoch Y. Park[*,‡], Masahiko Ikeuchi[†,§], Moritoshi Sato[†,§] and Rei Narikawa[*,†,‡,#]

[*]Graduate School of Integrated Science and Technology, Shizuoka University, 836 Ohya, Suruga, Shizuoka 422-8529, Japan

[†]Core Research for Evolutional Science and Technology, Japan Science and Technology Agency, 4-1-8 Honcho, Kawaguchi, Saitama 332-0012, Japan

[‡]Research Institute of Green Science and Technology, Shizuoka University, 836 Ohya, Suruga, Shizuoka 422-8529, Japan

[§]Graduate School of Arts and Sciences, University of Tokyo, 3-8-1 Komaba, Meguro, Tokyo 153-8902, Japan

[¶]AMED-PRIME, Japan Agency for Medical Research and Development, Tokyo, Japan

[#]To whom correspondence should be addressed.

Email: narikawa.rei@shizuoka.ac.jp, Tel: +81-54-238-4783

Short Title; Conversion of CBCR chromophore selectivity

Classification; BIOLOGIAL SCIENCES, Biochemistry

Keywords; bilin, *in vivo* imaging, protein engineering

Significance Statement

Although cyanobacteriochrome photoreceptors are potentially useful molecules for bio-imaging and optogenetics because of their compactness and spectral diversity, most cyanobacteriochromes have a drawback to need a chromophore unavailable in the mammalian cells. In order to overcome this significant drawback, this study focused on a mammalian intrinsic chromophore, biliverdin. We succeeded in conversion of biliverdin-rejective cyanobacteriochromes into BV-acceptable molecules by replacement of only four residues. Furthermore, molecular basis for the biliverdin incorporation has been revealed by the X-ray crystallography. One of such engineered molecules was shown to function as a near-infrared fluorescent probe for *in vivo* imaging in living mice. This study would provide rational strategy to obtain molecules applicable to bio-imaging and optogenetics.

Abstract

Because cyanobacteriochrome photoreceptors need only a single compact domain for chromophore incorporation and for absorption of visible spectra including long-wavelength far-red region, these molecules have been paid much attention for application to bio-imaging and optogenetics. Most cyanobacteriochromes, however, have a drawback to incorporate phycocyanobilin that is not available in the mammalian cells. In this study, we focused on biliverdin IXα (BV) that is a mammalian intrinsic chromophore and absorbs far-red region and revealed that replacement of only four residues was enough for conversion from BV-rejective cyanobacteriochromes into BV-acceptable molecules. We succeeded in determining the crystal structure of one of such engineered molecules, AnPixJg2_BV4, at 1.6 Å resolution. This structure identified unusual covalent bond linkage, which resulted in deep BV insertion into the protein pocket. The four mutated residues contributed reducing steric hindrances derived from the deeper insertion. We introduced these residues into other domains, and one of them, NpF2164g5_BV4, produced bright near-infrared fluorescence from mammalian liver *in vivo*. Collectively, this study provides not only molecular basis to incorporate BV by the cyanobacteriochromes but also rational strategy to open the door for application of cyanobacteriochromes to visualization and regulation of deep mammalian tissues.

/body

Introduction

Phytochromes are photoreceptors that are widely distributed among various organisms and that can incorporate a linear tetrapyrrole chromophore (also called bilin pigment). Among these, bacteriophytochromes bind to biliverdin IXα (BV) (SI Appendix, Fig. S1A) and exhibit red/far-red reversible photoconversion. BV is an intrinsic chromophore in mammalian cells that absorbs the longest wavelengths of far-red light among the natural bilin pigments identified to date. Longer light wavelengths facilitate deeper penetration into tissues while causing only low levels of damage (1); therefore, bacteriophytochromes have been utilized recently to develop optogenetic (2–4) and bio-imaging (5–10) tools. However, most bacteriophytochromes have a drawback, especially for use as optogenetic tools, in that they require three domains containing a conserved cGMP-phosphodiesterase/adenylate cyclase/FhlA (GAF) domain for BV incorporation.

Conversely, cyanobacteriochromes (CBCRs), which are cyanobacterial photoreceptors, require only a GAF domain for linear tetrapyrrole incorporation (11). The CBCR GAF domains covalently attach to the chromophore (SI Appendix, Fig. S1A, B) via a conserved canonical Cys residue within the GAF domain. Light-induced *Z*/*E* isomerization of a double bond between the C15 and C16 positions of the chromophore triggers reversible photoconversion between the dark state (15*Z* isomer) and the photoproduct (15*E* isomer) (SI Appendix, Fig. S1A, B). Recently, diverse natural CBCR GAF domains have been identified and phylogenetic analysis has clustered them into several lineages (12–17). Among these, CBCR GAF domains categorized in the expanded red/green (XRG) lineage are widely distributed and highly diverse in their spectral properties. Typical XRG CBCR GAF domains, including AnPixJg2, covalently attach to phycocyanobilin (PCB) and exhibit reversible photoconversion between a red light-absorbing form (Pr) with a 15*Z*-isomer and a green light-absorbing form (Pg) with a 15*E*-isomer (SI Appendix, Fig. S1B) (12). Its structure and detailed photoconversion mechanism have been elucidated by X-ray crystallography and various spectroscopic methods (18–24), revealing that crucial residues near the chromophore form an elaborate network with PCB to stabilize chromophore conformation (22, 24).

Recently, we have reported two novel XRG CBCR GAF domains, AM1_C0023g2 (25) and AM1_1557g2 (26), isolated from the chlorophyll *d*-containing cyanobacterium *Acaryochloris marina* that utilizes red-shifted far-red light as an energy source. These GAF domains covalently bind not only PCB but also BV, and upon BV-binding they can reversibly photoconvert between far-red light-absorbing forms (Pfr) with 15*Z*-isomers and orange light-absorbing forms (Po) with 15*E*-isomers (SI Appendix, Fig. S1A). These molecules are highly exceptional and no such molecules have not been reported to date. This red-shifted property may be because of the co-evolution of photosynthesis and light perception to adapt to a far-red light environment. Thus, if we could decipher the molecular mechanism of BV incorporation into these proteins, not only would we understand the unique strategy of *A. marina*'s adaptation to a far-red light environment, but we may also be able to introduce BV-binding capability into the other domains with unique spectral properties that would be advantageous for the development of optogenetics and bio-imaging technologies.

In this context, based on sequence comparison and structural information, we rationally introduced mutations into AnPixJg2 to confer BV-binding capability. Although no such rational trials to alter chromophore selectivity have not been succeeded yet including studies on the canonical phytochromes, we could figure out that replacement of only four residues on AnPixJg2 was enough for conversion from BV-rejective molecule into BV-acceptable molecule. Furthermore, crystal structure of the BV-binding AnPixJg2 variant in Pfr form revealed that these four residues cooperatively worked for efficient BV incorporation in atomic resolution. Based on these findings, we further succeeded in producing BV-binding variants by introducing these four residues into the other XRG CBCR GAF domains and demonstrated applicability of one of these molecules to bio-imaging *in vivo*. Thus, this study should provide rational strategy to obtain molecules for future application in optogenetics and bio-imaging because of their compact sizes and unique spectral properties.

Results

Identification of crucial residues for BV incorporation

To check whether or not AnPixJg2 could incorporate BV, His-tagged AnPixJg2 was purified from the BV-producing *Escherichia coli*. Although AnPixJg2 could bind BV and showed reversible photoconversion between a Pfr form with an absorbance maximum at 698 nm and a Po form with a maximum at 614 nm, the binding efficiency was quite low (3.7% ± 1.9) compared with AM1_C0023g2 (70%) and AM1_1557g2 (40%) (Fig. 1A, B, Table 1 and SI Appendix, Fig. S2A, B) (25, 26). We have also reported that BV-binding efficiency of AM1_1870g3 is as low as that of AnPixJg2 (27). These facts suggest that a sequence comparison based on the AnPixJg2 structure (24) may provide clues to the molecular mechanism of BV incorporation. From this comparison, we found that nine residues were specifically conserved between AM1_C0023g2 and AM1_1557g2 within 6 Å of the chromophore, namely Val273, Gln307, Tyr310, Lys318, Thr325, Ser334, Tyr335, Asp337 and Val353 in AM1_C0023g2. These correspond to residues Ala256, Glu290, His293, Arg301, Phe308, Gly317, His318, Ser320 and Ile336 in AnPixJg2 (SI Appendix, Fig. S1C, D). Among these, the Ser334/Gly317 position has already been shown to be important for BV-binding in AM1_C0023g2, and replacement of Ser334 with Gly improves the stability of the BV-binding holoprotein (25). This suggests that Gly317 in AnPixJg2 is potentially important for BV-binding capability. Therefore, we focused on the other eight residues in AnPixJg2 (details of the Gly/Ser position are given in the section of “Gly/Ser position” in the SI Appendix) and performed individual site-directed mutageneses on AnPixJg2: $A_{256}V$, $E_{290}Q$, $H_{293}Y$, $R_{301}K$, $F_{308}T$, $H_{318}Y$, $S_{320}D$ and $I_{336}V$. All *E. coli* cells expressing these variants exhibited similar colors and were visually indistinguishable to those expressing the wild type protein (SI

Appendix, Fig. S1E).

Thus, we constructed a mutant, in which the eight residues of AnPixJg2 were simultaneously replaced with the corresponding residues conserved between AM1_C0023g2 and AM1_1557g2. The mutant, AnPixJg2_BV8 (A$_{256}$V, E$_{290}$Q, H$_{293}$Y, R$_{301}$K, F$_{308}$T, H$_{318}$Y, S$_{320}$D and I$_{336}$V), exhibited significant improvement in BV incorporation with retaining far-red/orange reversible photoconversion. To evaluate the BV incorporation capability of the variant proteins, we established two parameters: the BV-binding efficiency of purified protein and the expression enhancement of holoprotein relative to wild type protein (calculation details are described as Materials and Methods). The binding efficiency and expression enhancement of AnPixJg2_BV8 were 52.6 ± 9.1% and 52.6-fold ± 19.5, respectively (Fig. 1B, Table 1 and SI Appendix, Fig. S2A, B).

Based on the PCB-binding AnPixJg2 structure, the Ala256, Glu290 and Ser320 side chains are unlikely to be directly involved in chromophore binding (SI Appendix, Fig. S1C). Furthermore, we identified another BV-binding CBCR GAF domain, AM1_6305g2, from the cyanobacterium *A. marina* (SI Appendix, Fig. S3 and Table S1). This domain possesses a His instead of the Lys in AM1_C0023g2 and AM1_1557g2 at the position corresponding to Arg301 in AnPixJg2 (SI Appendix, Fig. S1D). Thus, we constructed a mutant, AnPixJg2_BV4 (H$_{293}$Y, F$_{308}$T, H$_{318}$Y and I$_{336}$V), in which the aforementioned four residues were reverted to originals. The mutant could bind BV, exhibited far-red/orange reversible photoconversion, and its binding efficiency and expression enhancement were 74.7% ± 13.0 and 75.7-fold ± 8.6, respectively, which were significantly higher than those of AnPixJg2_BV8 (Fig. 1B, C, Table 1 and SI Appendix, Fig. S2A, B). This suggests not only that the other four residues are dispensable for BV-binding, but that some were, in fact, inhibitory.

To reduce the number of mutagenized residues further, we constructed four kinds of mutant in which each mutated residue of AnPixJg2_BV4 was reverted back to the original: AnPixJg2_BV3$_{H293}$ (F$_{308}$T, H$_{318}$Y and I$_{336}$V), AnPixJg2_BV3$_{F308}$ (H$_{293}$Y, H$_{318}$Y and I$_{336}$V), AnPixJg2_BV3$_{H318}$ (H$_{293}$Y, F$_{308}$T and I$_{336}$V) and AnPixJg2_BV3$_{I336}$ (H$_{293}$Y, F$_{308}$T and H$_{318}$Y). All mutants exhibited far-red/orange reversible photoconversion (SI Appendix, Fig. S2A). The binding efficiencies of AnPixJg2_BV3$_{H293}$, AnPixJg2_BV3$_{F308}$, AnPixJg2_BV3$_{H318}$ and AnPixJg2_BV3$_{I336}$ were 54.2% ± 18.6, 4.0% ± 2.1, 41.4% ± 15.7 and 38.5% ± 13.8, respectively, while their expression enhancements were as 44.7 ± 4.0, 1.3 ± 0.3, 49.0 ± 3.4 and 22.5 ± 5.9-fold, respectively (Fig. 1B, Table 1 and SI Appendix, Fig. S2B). The binding efficiency and expression enhancement of all AnPixJg2_BV3 variants were significantly lower than those of AnPixJg2_BV4, but AnPixJg2_BV3$_{F308}$ exhibited largest reductions in both binding efficiency and expression enhancement, suggesting that it plays the most important role in BV-incorporation. Furthermore, AnPixJg2_BV3$_{I336}$ exhibited a larger defect in expression enhancement than AnPixJg2_BV3$_{H293}$ and AnPixJg2_BV3$_{H318}$, suggesting that the I$_{336}$V replacement may play a more important role than the H$_{293}$Y and H$_{318}$Y replacements. This consideration prompted us to construct AnPixJg2_BV2 (F$_{308}$T and I$_{336}$V). AnPixJg2_BV2 bound BV with a 37.8% ± 21.3 binding efficiency and 23.1-fold ± 7.4 expression enhancement and exhibited far-red/orange reversible photoconversion (Fig. 1B, Table 1 and SI Appendix, Fig. S2A, B). Although its binding efficiency and expression enhancement were slightly lower than those of AnPixJg2_BV3$_{H293}$ and AnPixJg2_BV3$_{H318}$, AnPixJg2_BV2 maintained a moderately high BV-incorporation capability compared with the wild type protein. Furthermore, we had already constructed AnPixJg2_F$_{308}$T and AnPixJg2_I$_{336}$V, and had found that their BV-binding efficiencies

(10.1% ± 10.1 and 13.0% ± 6.7, respectively) and expression enhancements (3.5 ± 1.0 and 5.5 ± 0.8-fold, respectively) were significantly lower than those of AnPixJg2_BV2 (Fig. 1B, Table 1 and SI Appendix, Fig. S2A, B). Collectively, these results indicated that the residues Tyr293, Thr308, Tyr318 and Val336 are essential for BV incorporation, with Thr308 and Val336 are likely to be more critical than Tyr293 and Tyr318. In conclusion, AnPixJg2_BV4 is the variant that exhibits the most efficient and stable BV incorporation. The section of "Spectral comparison of AnPixJg2 and its variants" in the SI Appendix presents the details of the spectral properties of these variant proteins (Table 1 and SI Appendix, Fig. S2A, C, D).

Structural insights into BV incorporation

To obtain direct insights into the molecular mechanism of BV incorporation, we determined the crystal structure (1.6 Å resolution) of the Pfr form of AnPixJg2_BV4 (SI Appendix, Fig. S4A-C and Table S2, see the section of "Crystal structure determination" in the SI Appendix for details), which exhibited the best BV incorporation among the AnPixJg2 variants. The overall structure of BV-bound AnPixJg2_BV4 was quite similar to that of PCB-bound AnPixJg2 (the root mean square deviation was 0.908 Å for the Cα atoms of residues 233–388) except that the N-terminal α-helix was oriented in the opposite direction, which may be an artifact derived from crystal packing (SI Appendix, Fig. S4D, E). Notably, electron density maps ($2|F_o|-|F_c|$) clearly showed that the canonical Cys residue (Cys321) of AnPixJg2_BV4 bound to $C3^2$ position in the vinyl group of BV, whereas that of AnPixJg2 bound to $C3^1$ position in the ethylidene group of PCB (Fig. 2A, B and SI Appendix, Fig. S4D, E). Because additional carbon ($C3^2$) was inserted in the covalent bond linkage between the C3 of the A ring and the sulfur atom of Cys321, the

BV incorporated into AnPixJg2_BV4 shifted relative to the PCB of the WT structure, in which the shifting was calculated as about 0.75 Å. It is of note that the ring C shifted toward the β-sheets of the chromophore binding pocket compared to the PCB incorporated into AnPixJg2 (Fig. 2C). Nevertheless, the structural arrangements of five residues (Trp289, Asp291, Arg301, His322 and Tyr352) reported to be important for chromophore stability (24) were highly conserved between these two structures (Fig. 2A, B and SI Appendix, Fig. S4F, G, shown as yellow green and deep pink, respectively). Although Tyr352 was located at the β-sheets, its interaction partner, the D ring carbonyl group, hardly shifted toward the β-sheets, and so this interaction should be conserved between these two structures. Arg301 participated in chromophore binding in different ways in the two proteins. In AnPixJg2_BV4, it stabilized the ring C propionate of BV by hydrogen bonding via a water molecule, whereas in AnPixJg2 it directly interacted with the same propionate of PCB by hydrogen bonds.

Notably, although the side chains of the four mutation sites (His293, Phe308, His318 and Ile336) were positioned around ring C of the chromophores in both structures, the protein-chromophore interactions of these side chains were totally different between these two structures (Fig. 2A, B and SI Appendix, Fig. S4F, G, shown as blue green and deep red, respectively). In the Phe/Thr308 and Ile/Val336 positions, the bulky Phe308 and Ile336 residues of AnPixJg2 held the C ring by hydrophobic interactions (Fig. 2D, lower). Because these residues were located at the β-sheets around the C ring, these residues should be affected by the chromophore shifting. The fact that AnPixJg2 could not efficiently bind BV means that these bulky residues may cause steric hindrance of the C ring, which is largely shifted toward the β-sheets in comparison to that of PCB (Fig. 2C). This interpretation is supported by the superimposition of BV on the AnPixJg2 structure (Fig. 2D, middle). Conversely, the compact Thr308 and Val336 residues of AnPixJg2_BV4 avoided steric hindrance with the C ring (Fig. 2D, upper). It is noteworthy that the ring C propionate of BV was in a vertical direction toward the B–C plane, whereas that of PCB lay parallel with the plane (Fig. 2A, B). This suggests that not only replacement with compact residues, but also a flexible rearrangement of the ring C propionate, is important for BV incorporation (Fig. 2A, B). In this context, the other replacements at the His/Tyr293 and His/Tyr318 positions contribute to the rearrangement (Fig. 2A, B and SI Appendix, Fig. S4F, G). The His318 of AnPixJg2 interacted with the ring B propionate of PCB by a direct hydrogen bond, while the Tyr318 of AnPixJg2_BV4 directly hydrogen bonded with the ring C propionate of BV. The His293 of AnPixJg2 stabilized the ring C propionate of PCB by hydrogen bonding via a water molecule, while Tyr293 of AnPixJg2_BV4 did not form any hydrogen bonds with the chromophore. These distinctive interaction networks should facilitate “parallel” and “vertical” conformations of the ring C propionate. Namely, replacement of His318 with Tyr resulted in switching the interaction partner from the ring B propionate to the ring C propionate and directly contributed to the “vertical” conformation, whereas replacement of His293 with Tyr resulted in removal of hydrogen bonds with the ring C propionate to contribute to destabilization of the “parallel” conformation. Moreover, the hydroxy group of Thr308 indirectly hydrogen bonded with the ring C propionate of BV via a water molecule (Fig. 2A and SI Appendix, Fig. S4F), which also facilitated the “vertical” conformation. This indicates that replacement of Phe308 with Thr has effects not only on reduction of steric hindrance, but also on rearrangement of the ring C propionate, which is consistent with the fact that $F_{308}T$ replacement had the largest contribution on efficient BV incorporation (Fig. 1B and Table 1). In conclusion, these four residues in AnPixJg2_BV4 work cooperatively to solve problems triggered by chromophore shifting, resulting in stable BV incorporation.

Protein engineering of the other GAF domains

To expand our strategy to other CBCR GAF domains within the XRG lineage, we targeted several domains with a PCB chromophore that have atypical spectral properties: AnPixJg4 (Pg–to–Pr rapid dark reversion) (28); AM1_1186g2 (red/blue reversible photoconversion) (29); AM1_1870g3 (red-shifted red/green reversible photoconversion) (27); NpF2164g3 (violet/orange reversible photoconversion) (30); and NpF2164g5 (intense far-red fluorescence without photoconversion) (31). Because all these wild type proteins exhibit a little or no BV incorporation (Fig. 3A-C and SI Appendix, Fig. S5A-J and Table S1), we engineered these domains for BV incorporation based on the AnPixJg2_BV4 sequence (SI Appendix, Fig. S5K).

Introduction of mutations into AnPixJg4, AM1_1870g3 and NpF2164g5 significantly improved BV-binding efficiencies, which were 44%, 82% and 70%, respectively (Fig. 3A-C and SI Appendix, Fig. S5A-C, F-H and Table S1). In contrast, introduction of the same mutations into AM1_1186g2 and NpF2164g3, whose sequences near the chromophore are greatly diversified from those of typical XRG CBCR GAF domains including AnPixJg2, did not improve BV-binding efficiencies (SI Appendix, Fig. S5D, E, I, J and Table S1). AnPixJg4_BV4 exhibited Pfr-to-Po photoconversion and rapid Po-to-Pfr dark reversion, in which the half-life of the AnPixJg4_BV4 dark reversion was 2.8 s ± 0.1 at 25 ºC. This is about 400-fold faster than that of AnPixJg2_BV4 (1199 s ± 12.9 at 25 ºC) (Fig. 3A, D and SI Appendix, Fig. S5A). Faster dark reversion enables the regulation of biological activities by monochromatic far-red light illumination.

AM1_1870g3_BV4 exhibited far-red/orange reversible photoconversion, whose difference spectrum (Pfr – Po) possesses a positive peak at 718 nm, which is red-shifted by 18 nm compared with that of AnPixJg2_BV4 (Fig. 3B, E and SI Appendix, Fig. S5B). This red-shifted property is advantageous for optogenetic control within deep tissues in mammals. NpF2164g5_BV4 stably absorbed far-red light without photoconversion and exhibited fluorescence covering the near-infrared (NIR) region with a 4% quantum yield. Excitation and emission spectra of NpF2164g5_BV4 bound to BV peaked at 680 nm and 700 nm, respectively, and were red-shifted compared with those of NpF2164g5 bound to PCB (Fig. 3C, F and SI Appendix, Fig. S5C). It is of note that the fluorescence excitation spectrum showed a prominent shoulder at 641 nm, which may reflect heterogenous population. Detailed studies such as structure determination of this molecule is needed to understand this unique fluorescence property. In contrast, variant proteins based on AnPixJg2_BV2 and the AnPixJg2_BV3$_{\mathrm{H293}}$ sequences could not bind BV efficiently (SI Appendix, Fig. S5A-C). These results indicate that the "BV4" replacement is a robust engineering design for producing BV-binding capability.

Fluorescence imaging in living mice using NpF2164g5_BV4

We show that the compact NIR fluorescent protein, NpF2164g5_BV4, is applicable to *in vivo* imaging in living mice. To determine its applicability, we first tested whether the NIR fluorescence of NpF2164g5_BV4 could be observed in a live mammalian cell. COS-7 cells were transfected with NpF2164g5_BV4. After incubation with BV, the cells were imaged using a confocal fluorescence microscope. To quantitatively evaluate the NIR fluorescence of NpF2164g5_BV4, we fused it with green fluorescent protein (GFP) and normalized variations in its expression levels by dividing the NIR fluorescence by the

GFP fluorescence. The cells expressing NpF2164g5_BV4 exhibited bright NIR fluorescence compared to those expressing GFP as a negative control (Fig. 4A, B). Next, we examined whether the NIR fluorescence of NpF2164g5_BV4 could be imaged *in vivo* in living mice. We transiently transfected mice liver with NpF2164g5_BV4 by hydrodynamic tail vein (HTV) injection. The transfected mice were intravenously injected with BV and then imaged using an *in vivo* fluorescence imager. NIR fluorescence of NpF2164g5_BV4 was observed from the liver of the transfected mice (Fig. 4C, D). Additionally, the isolated liver from the transfected mice was confirmed to exhibit bright NIR fluorescence as compared to that from the uninjected mice (Fig. 4E, F). These results indicate that NpF2164g5_BV4 is applicable to *in vivo* fluorescence imaging of deep tissues of living mice.

We compared NpF2164g5_BV4 with iRFP, a near-infrared fluorescent protein widely used for *in vivo* fluorescence imaging (6). COS-7 cells transfected with iRFP were incubated with BV before imaging as in the case of NpF2164g5_BV4. iRFP has previously been engineered by extensive mutagenesis of a BV-bound bacteriophytochrome, *Rp*BphP2, such as $D_{202}H$ mutation to inhibit its photoconversion and additional 13 mutations including those around the D ring of BV to greatly increase its fluorescence (6). On the other hand, NpF2164g5_BV4 has mutations around the B and C rings for conferring BV-binding property, but has not yet been subjected to mutagenesis around the D ring of BV to improve its fluorescence. Nevertheless, the NIR fluorescence intensity of NpF2164g5_BV4 has already reached 20% of that of iRFP (Fig. 4A, B), suggesting that NpF2164g5_BV4 could be a platform to develop a powerful, compact NIR fluorescent probe for *in vivo* fluorescence imaging.

Discussion

In this study, we succeeded in rationally converting chromophore selectivity of several non-BV-binding CBCR GAF domains to accept BV by “BV4” replacement and elucidated its structural basis at atomic resolution (Fig. 1-3). We quantitatively evaluated BV-binding capability using two parameters; the BV-binding efficiency and the expression enhancement of the holoprotein. Although it is generally difficult to determine the absolute value of protein concentration using conventional methods, relative comparison between variant proteins is reliable because they share an almost identical amino acid composition. From such relative comparisons, AnPixJg2_BV4 was determined to be the best variant protein for BV incorporation among all the AnPixJg2 variant proteins tested (Fig. 1). This conclusion is supported further by the engineering of the other molecules (Fig. 3). Furthermore, we demonstrated that one of the BV-binding molecules, NpF2164g5_BV4, can function as a NIR fluorescent probe *in vivo* (Fig. 4). Because NpF2164g5_BV4 has not yet been engineered to improve fluorescence, this molecule could be a platform for the further development of brighter NIR fluorescent probes.

We have shown that few exceptional CBCR GAF domains from *A. marina*, namely AM1_1557g2 (26), AM1_C0023g2 (25) and AM1_6305g2, efficiently incorporate BV and possess the “BV4” residues as part of their native sequences (SI Appendix, Fig. S5K). Thus, molecular mechanism used by these natural domains to incorporate BV should be similar to that of AnPixJg2_BV4, suggesting that acquisition of these four residues during evolution enables *A. marina* to sense longer wavelengths of far-red light. Very recently, it has been reported that *Acaryochloris thomasi* lacks chlorophyll *d*, although this species clearly belongs to the genus *Acaryochloris* and is phylogenetically close to *A. marina*

(32). Only this species within this genus lacks chlorophyll *d*, indicating that this strain lost chlorophyll *d* during evolution. Because this species utilizes red rather than far-red light as an energy source, we speculate that GAF domains from this species may also have lost BV-binding capability. To assess this possibility, we searched for domains homologous to AM1_1557g2 from its draft genome sequence and identified two candidates (C1752_03750g3 and C1752_03750g4; SI Appendix, Fig. S5K). Interestingly, three of the four "BV4" residues are not conserved in these domains (SI Appendix, Fig. S5K), strongly indicating that they cannot efficiently incorporate BV. This might be a clue to the co-evolution of photosynthesis and light perception. We could not find any other CBCR GAF domains with these "BV4" residues from other cyanobacterial lineages, including chlorophyll *f*-containing cyanobacteria, which also utilize far-red light as an energy source (33). In this context, the acquisition and loss of BV-binding capability by CBCR GAF domains may be restricted only to the genus *Acaryochloris*. Otherwise, further genomic analyses of unknown or uncharacterized cyanobacterial species would provide another examples for the BV-binding molecules in the future.

To date, developmental platforms for BV-binding tools have been restricted to bacteriophytochromes (2–10) and photosynthetic light-harvesting proteins (9, 34). The rational strategy to confer BV-binding capability to the CBCRs provided by this study has been applicable to both non-photoconvertible and photoconvertible molecules. Thus, this strategy may contribute to the development of new bio-imaging and optogenetic tools in the future. In this context, our findings open a new CBCR avenue to the BV-based optical field. The compactness, photoreversibility and remarkable spectral diversity of the CBCR superfamily should ensure unique BV-based development of optical tools that cannot be achieved by conventional platforms that have less diversity.

Materials and Methods

Materials and methods for bacterial cell culture, bioinformatics, plasmid constructions, protein expression and purification, electrophoresis, crystallization and structure determination, mammalian cell culture and transfection, confocal fluorescence imaging, mice, and spectral unmixing and data analysis are described in the supplementary materials.

Biochemical characterization of cyanobacteriochromes

For the denaturation assay, both the dark state (15*Z*-isomer) and photoproduct (15*E*-isomer) of the native proteins were 5-fold diluted into 7 M guanidinium chloride (GdmCl)/1% (v/v) HCl and absorption spectra recorded at room temperature before and after 3 min of illumination with white light.

To monitor photoconversion and dark reversion processes, absorbance at 698 nm against red light (700 nm) was measured for AnPixJg2_BV4 and AnPixJg4_BV4 for 2 min with dark intervals of 5 min at 25 ºC. Half-lives were calculated from the dark reversion kinetics.

To calculate BV-binding efficiency, we measured the absorbance spectra of *Z*-isomers of free BV (Frontier Scientific) at various concentrations and constructed a standard curve. Using this standard curve, we calculated BV-binding efficiencies of various proteins based on the absorbance values of *Z*-isomers at 700 nm denatured by 7 M GdmCl/1% (v/v) HCl.

To estimate the relative expression enhancements of the holoproteins (AnPixJg2 and its mutants) expressed in *E. coli* C41 pKT270, lysates were illuminated with orange light (620 nm and 600 nm) and the holoproteins purified in the Pfr form under dark conditions using an NGC Chromatography System (BIO-RAD). Enhancements were estimated based on the area of each peak monitored by absorbance at 700 nm during chromatography and normalized to fresh cell weight.

The molar extinction coefficients of the dark state and photoproduct of the native proteins were calculated from each absorbance value at the peak wavelength per the molar concentration of the holoprotein as determined by Bradford assay.

Fluorescence imaging of living mice and the isolated liver

The mice were transfected with GFP-NpF2164g5_BV4 by hydrodynamic tail vein (HTV) injection using TransIT-EE Hydrodynamic Delivery Solution (Mirus) according to the manufacturer's instructions. As a negative control, we used uninjected mice. Twenty-three hours after the HTV injection, both the HTV-injected and uninjected mice were intravenously injected with BV (50 nmol/g mouse weight), and the abdominal hair of them was removed using a depilatory cream. One hour after the BV injection, the mice were anesthetized with isoflurane (Wako), and imaged with Lumazone *in vivo* imaging system (Shoshin EM) equipped with an EMCCD camera (Evolve 512, Photometrics) and an emission filter, ET700/75m (Chroma). As an excitation light source, a liquid-cooled high-output LED light source (LAMBDA HPX, Shutter instrument) with a tunable filter changer (LAMBDA VF-5, Shutter instrument) was used. Fluorescence images were obtained in two channels: channel 1 was acquired with 570 ± 7 nm excitation (1.05 W/m^2 at the specimen) and 700 ± 37.5 nm emission, and channel 2 was acquired with 630 ± 6.5 nm excitation (0.53 W/m^2 at the specimen) and 700 ± 37.5 nm emission. The exposure time was 100 msec, and the camera parameters for gain and intensification were set to 1 and 100, respectively. After the *in vivo* imaging, the liver was isolated from the mice using standard surgical procedure, and imaged under the same imaging channels and conditions as the *in vivo* imaging. Additionally, to verify the expression of GFP-NpF2164g5_BV4, its GFP fluorescence in the isolated liver was also determined using a fluorescence stereo zoom microscope (Axio Zoom.V16, Carl Zeiss) equipped with a filter set for GFP (filter set 38 HE, Carl Zeiss).

Acknowledgements

We thank Prof. M. Yazawa (Columbia University) and Dr. G. Enomoto (University of Freiburg) for helpful discussion. The authors would like to thank Enago (www.enago.jp) for the English language review. We also thank the staff of the Photon Factory for the X-ray data collection. This research was approved by the Photon Factory Program Advisory Committee (Proposal No. 2017G051). This work was supported by JST, CREST (JPMJCR1653 to M.I., M.S. and R.N.), and JSPS KAKENHI (26702036 to R.N.). K.S. was supported by Grant-in-Aid for JSPS Research Fellow (18J01772).

Author contributions

K.F., M.I., M.S. and R.N. designed the research. K.F. performed plasmid construction, protein purification, protein crystallization, biochemical studies and spectral analyses. T.M. and E.Y.P. performed X-ray analyses and model construction. Y.K., T.N., K.S. and Y.U. performed imaging analyses *in vitro* and *in vivo*. T.Y., K.M. and Y.T. performed plasmid construction, protein purification and spectral analyses for several proteins. J.-H.C. and H.K. performed biochemical studies. K.F., T.M., Y.K., T.N., M.S. and R.N. analyzed the data and wrote the manuscript.

Data depositions

The coordinates and structure factor for AnPixJg2_BV4 containing BV have been deposited in the Protein Data Bank under accession code 5ZOH.

References

1. Ziegler T, Möglich A (2015) Photoreceptor engineering. *Front Mol Biosci* 2:30.

2. Gasser C, et al. (2014) Engineering of a red-light-activated human cAMP/cGMP-specific phosphodiesterase. *Proc Natl Acad Sci USA* 111(24):8803–8808.

3. Ryu M-H, et al. (2014) Engineering adenylate cyclases regulated by near-infrared window light. *Proc Natl Acad Sci USA* 111(28):10167–10172.

4. Redchuk TA, Omelina ES, Chernov KG, Verkhusha VV (2017) Near-infrared optogenetic pair for protein regulation and spectral multiplexing. *Nat Chem Biol* 13(6):633–639.

5. Shu X, et al. (2009) Mammalian expression of infrared fluorescent proteins engineered from a bacterial phytochrome. *Science* 324(5928):804–807.

6. Filonov GS, et al. (2011) Bright and stable near-infrared fluorescent protein for in vivo imaging. *Nat Biotechnol* 29(8):757–761.

7. Baloban M, et al. (2017) Designing brighter near-infrared fluorescent proteins: insights from structural and biochemical studies. *Chem Sci* 8(6):4546–4557.

8. Bhattacharya S, Auldridge ME, Lehtivuori H, Ihalainen JA, Forest KT (2014) Origins of fluorescence in evolved bacteriophytochromes. *J Biol Chem* 289(46):32144–32152.

9. Rodriguez EA, et al. (2016) A far-red fluorescent protein evolved from a cyanobacterial phycobiliprotein. *Nat Methods* 13(9):763–769.

10. Buhrke D, et al. (2016) The role of local and remote amino acid substitutions for optimizing fluorescence in bacteriophytochromes: A case study on iRFP. *Sci Rep* 6:28444.

11. Ikeuchi M, Ishizuka T (2008) Cyanobacteriochromes: a new superfamily of tetrapyrrole-binding photoreceptors in cyanobacteria. *Photochem Photobiol Sci* 7(10):1159–1167.

12. Narikawa R, Fukushima Y, Ishizuka T, Itoh S, Ikeuchi M (2008) A novel photoactive GAF domain of cyanobacteriochrome AnPixJ that shows reversible green/red photoconversion. *J Mol Biol* 380(5):844–855.

13. Hirose Y, Shimada T, Narikawa R, Katayama M, Ikeuchi M (2008) Cyanobacteriochrome CcaS is the green light receptor that induces the expression of phycobilisome linker protein. *Proc Natl Acad Sci USA* 105(28):9528–9533.

14. Yoshihara S, Katayama M, Geng X, Ikeuchi M (2004) Cyanobacterial phytochrome-like PixJ1 holoprotein shows novel reversible photoconversion between blue- and green-absorbing forms. *Plant Cell Physiol* 45(12):1729–1737.

15. Rockwell NC, Martin SS, Lagarias JC (2016) Identification of cyanobacteriochromes detecting far-red light. *Biochemistry* 55(28):3907–3919.

16. Rockwell NC, Martin SS, Gulevich AG, Lagarias JC (2012) Phycoviolobilin formation and spectral tuning in the DXCF cyanobacteriochrome subfamily. *Biochemistry* 51(7):1449–1463.

17. Fushimi K, et al. (2016) Cyanobacteriochrome photoreceptors lacking the canonical Cys residue. *Biochemistry* 55(50):6981–6995.

18. Song C, Narikawa R, Ikeuchi M, Gärtner W, Matysik J (2015) Color tuning in red/green cyanobacteriochrome AnPixJ: photoisomerization at C15 causes an excited-state destabilization. *J Phys Chem B* 119(30):9688–9695.

19. Velazquez Escobar F, et al. (2013) Photoconversion mechanism of the second GAF domain of cyanobacteriochrome AnPixJ and the cofactor structure of its green-absorbing state. *Biochemistry* 52(29):4871–4880.

20. Kim PW, et al. (2012) Femtosecond photodynamics of the red/green cyanobacteriochrome NpR6012g4 from Nostoc punctiforme. 1. Forward dynamics. *Biochemistry* 51(2):608–618.

21. Kim PW, et al. (2012) Femtosecond photodynamics of the red/green cyanobacteriochrome NpR6012g4 from Nostoc punctiforme. 2. reverse dynamics. *Biochemistry* 51(2):619–630.

22. Lim S, et al. (2018) Correlating structural and photochemical heterogeneity in cyanobacteriochrome NpR6012g4. *Proc Natl Acad Sci USA* 115(17):4387–4392.

23. Xu X-L, et al. (2014) Combined mutagenesis and kinetics characterization of the bilin-binding GAF domain of the protein Slr1393 from the Cyanobacterium *Synechocystis* PCC6803. *Chembiochem* 15(8):1190–1199.

24. Narikawa R, et al. (2013) Structures of cyanobacteriochromes from phototaxis regulators AnPixJ and TePixJ reveal general and specific photoconversion mechanism. *Proc Natl Acad Sci USA* 110(3):918–923.

25. Fushimi K, et al. (2016) Photoconversion and fluorescence properties of a red/green-type cyanobacteriochrome AM1_C0023g2 that binds not only phycocyanobilin but also biliverdin. *Front Microbiol* 7:588.

26. Narikawa R, et al. (2015) A biliverdin-binding cyanobacteriochrome from the chlorophyll *d*-bearing cyanobacterium *Acaryochloris marina*. *Sci Rep* 5:7950.

27. Narikawa R, Fushimi K, Ni-Ni-Win, Ikeuchi M (2015) Red-shifted red/green-type cyanobacteriochrome AM1_1870g3 from the chlorophyll *d*-bearing cyanobacterium *Acaryochloris marina*. *Biochem Biophys Res Commun* 461(2):390–395.

28. Fushimi K, Enomoto G, Ikeuchi M, Narikawa R (2017) Distinctive properties of dark reversion kinetics between two red/green-type cyanobacteriochromes and their application in the photoregulation of cAMP synthesis. *Photochem Photobiol* 93(3):681–691.

29. Narikawa R, Enomoto G, Ni-Ni-Win, Fushimi K, Ikeuchi M (2014) A new type of dual-Cys cyanobacteriochrome GAF domain found in cyanobacterium *Acaryochloris marina*, which has an unusual red/blue reversible photoconversion cycle. *Biochemistry* 53(31):5051–5059.

30. Rockwell NC, Martin SS, Feoktistova K, Lagarias JC (2011) Diverse two-cysteine photocycles in phytochromes and cyanobacteriochromes. *Proc Natl Acad Sci USA* 108(29):11854–11859.

31. Rockwell NC, Martin SS, Lagarias JC (2012) Red/green cyanobacteriochromes: sensors of color and power. *Biochemistry* 51(48):9667–9677.

32. Partensky F, et al. (2018) A novel species of the marine cyanobacterium *Acaryochloris* with a unique pigment content and lifestyle. *Sci Rep* 8(1):9142.

33. Gan F, Bryant DA (2015) Adaptive and acclimative responses of cyanobacteria to far-red light. *Environ Microbiol* 17(10):3450–3465.

34. Ding W-L, et al. (2017) Small monomeric and highly stable near-infrared fluorescent markers derived from the thermophilic phycobiliprotein, ApcF2. *Biochim Biophys Acta* 1864(10):1877–1886.

Figure Legends

Figure 1. Protein engineering of AnPixJg2 for BV incorporation. (A) Phenotypes of non-engineered AnPixJg2 wide type. Upper left: *E. coli* cell pellet, upper right: color change of a solution upon irradiation with far-red or orange light, lower: normalized absorption spectra of the dark state (Pfr form, dark red) and the photoproduct (Po form, orange). (B) BV-binding efficiencies (upper, deep pink) and relative expression enhancements (lower, light blue) of AnPixJg2 and its variants. Efficiencies were estimated based on the protein and chromophore concentrations (mean ± standard deviation, $n = 5$). Enhancements were estimated based on the absorbance peak area at 700 nm during chromatography and normalized to fresh cell weight (mean ± standard deviation, $n = 4$). Details were given in the Materials and Methods. Data were analyzed statistically by Student *t*-test (P-values: $* < 0.05$ and $** < 0.01$, respectively). (C) Phenotypes of engineered AnPixJg2_BV4. Upper left: *E. coli* cell pellet, upper right: color change of a solution upon irradiation with far-red or orange light, lower panel: normalized absorption spectra of the dark state and the photoproduct.

Figure 2. Crystal structure of the Pfr form of AnPixJg2_BV4 bound to BV (PDB ID: 5ZOH) compared with that of the Pr form of AnPixJg2 bound to PCB (PDB ID: 3W2Z). (A, B) Structural arrangements of conserved and “BV4” residues in AnPixJg2_BV4 (deep pink and deep red, respectively) and AnPixJg2 (yellow green and blue green, respectively). (C) Structural comparison between BV (light green) and PCB (blue) with the canonical the Cys (Cys321) shown as stick model with showing β-sheets as ribbon model. (D) Space-filling models of the chromophores with Phe/Thr308 and Ile/Val336 residues: AnPixJg2_BV4 (upper), superimposition of BV on AnPixJg2 (middle) and AnPixJg2 (lower).

Figure 3. Protein engineering of other XRG CBCR GAF domains for BV incorporation. (A) Normalized absorption spectra of the dark states (Pfr form, dark red) and the photoproducts (Po form, orange) of AnPixJg4 (dotted) and its BV4 variant bound to BV (solid). (B) Normalized absorption spectra of the dark states and the photoproducts of AM1_1870g3 (dotted) and its BV4 variant bound to BV (solid). (C) Normalized absorption spectra of the dark states of NpF2164g5 (dotted) and its BV4 variant bound to BV (solid). (D) Normalized absorbance changes of AnPixJg4_BV4 (yellow) and AnPixJg2_BV4 (green) during a light-to-dark transition. The half-lives of AnPixJg4_BV4 and AnPixJg2_BV4 were 2.8 s ± 0.1 and 1199 s ± 12.9 (mean ± standard division, n = 3) at 25 ºC, respectively. (E) Normalized difference absorption spectra (Pfr – Po) of AM1_1870g3_BV4 (red) and AnPixJg2_BV4 (green). The positive peaks were at 718 nm and 700 nm, respectively. (F) Normalized fluorescence excitation (blue) and fluorescence emission spectra (red) of NpF2164g5_BV4 bound to BV (deep colors) and NpF2164g5 bound to PCB (light colors). The fluorescence excitation and emission peaks of BV-bound NpF2164g5_BV4 were at 680 nm and 700 nm, respectively, while those of PCB-bound NpF2164g5 were at 637 nm and 656 nm, respectively.

Figure 4. Fluorescence imaging in living mammalian cells and mice using NpF2164g5_BV4. (A) Confocal fluorescence images of COS-7 cells transfected with GFP-NpF2164g5_BV4 (left), GFP as a negative control (middle), or GFP-iRFP (right). NIR fluorescence was detected at 640 nm upon excitation at 633 nm. GFP fluorescence was detected at 500 nm upon excitation at 488 nm. The color bar below each image indicates the range of fluorescence intensity (FI). Scale bar, 20 μm. Representative images from three independent experiments (n = 24). (B) NIR fluorescence intensities of COS-7 cells transfected with GFP-NpF2164g5_BV4, GFP as a negative control, or GFP-iRFP. To normalize variations in their expression levels among the transfected cells, NIR fluorescence was divided by GFP fluorescence. Data are shown as the mean ± standard deviation (n = 24, from three independent experiments). Numbers above bars indicate the mean values. Data were analyzed statistically by two-tailed Welch's *t*-test (P-value: * < 0.05). (C) Overlay of light and NIR fluorescence images of living mice. Left: transfected mouse with GFP-NpF2164g5_BV4, right: uninjected mouse as a negative control. The NIR fluorescence images were acquired with excitation at 630 ± 6.5 nm and emission at 700 ± 37.5 nm, and spectrally unmixed to extract the NIR fluorescence from autofluorescence of mouse tissues. Details are given in the Materials and Methods. Fluorescence intensities are shown in pseudocolor. Representative images from two independent experiments (n = 3). (D) Fluorescence intensities of the liver of living mice that were transfected with GFP-NpF2164g5_BV4 or uninjected (mean ± standard deviation, n = 3, from two independent experiments). Data were analyzed statistically by two-tailed Welch's *t*-test (P-value: * < 0.05). (E) NIR fluorescence images of the isolated liver from transfected mouse (upper) and uninjected mouse (lower). Left: light image, right: NIR fluorescence image acquired with excitation at 630 ± 6.5 nm and emission at

700 ± 37.5 nm. Fluorescence intensities are shown in pseudocolor. Scale bar, 1 cm. Representative images from two independent experiments (n = 3). (F) Fluorescence intensities of the isolated liver from mice that were transfected with GFP-NpF2164g5_BV4 or uninjected (mean ± standard deviation, n = 3, from two independent experiments). Data were analyzed statistically by two-tailed Welch's *t*-test (P-value: * < 0.05).

Fig. 1

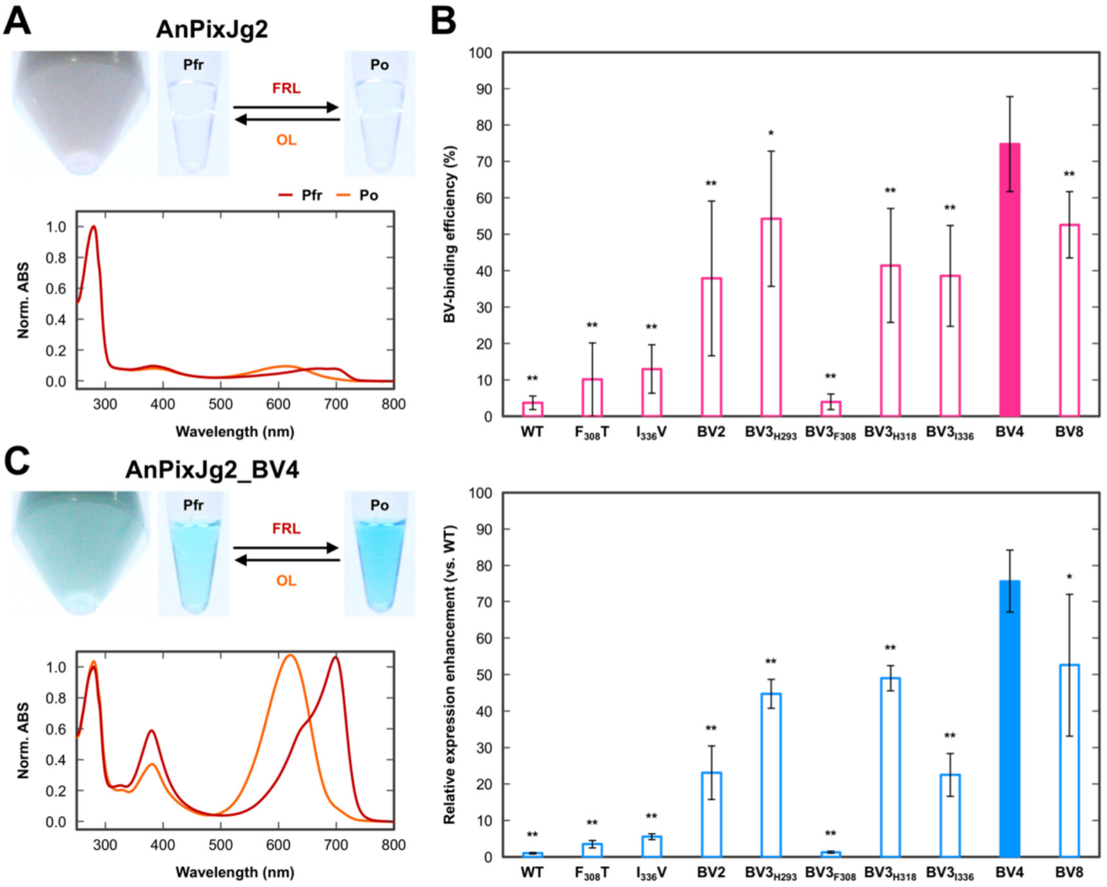
A
AnPixJg2
Pfr
FRL
OL
Po
Pfr
Po
1.0
0.8
0.6
0.4
0.2
0.0
Norm. ABS
300
400
500
600
700
800
Wavelength (nm)
B
100
90
80
70
60
50
40
30
20
10
0
BV-binding efficiency (%)
**
*
WT
F$_{308}$T
I$_{336}$V
BV2
BV3$_{H293}$
BV3$_{F308}$
BV3$_{H318}$
BV3$_{I336}$
BV4
BV8
C
AnPixJg2_BV4
Pfr
FRL
OL
Po
Norm. ABS
Wavelength (nm)
Relative expression enhancement (vs. WT)

Fig. 2

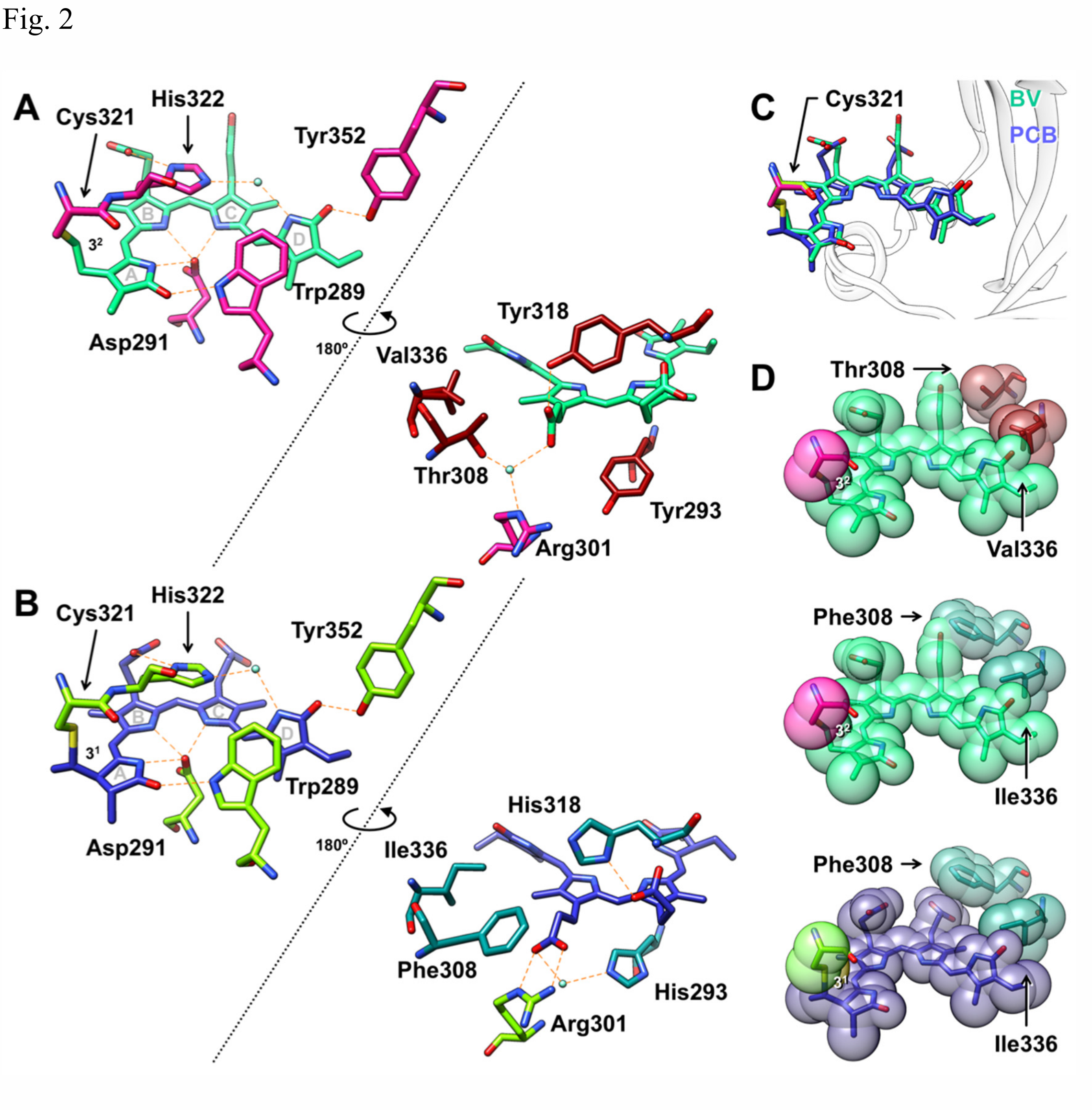
A
Cys321
His322
Tyr352
B
C
D
A
3²
Trp289
Asp291
180º
Val336
Tyr318
Thr308
Tyr293
Arg301
B
Cys321
His322
Tyr352
B
C
D
A
3¹
Trp289
Asp291
180º
Ile336
His318
Phe308
His293
Arg301
C
Cys321
BV
PCB
D
Thr308
3²
Val336
Phe308
3²
Ile336
Phe308
3¹
Ile336

Fig. 3

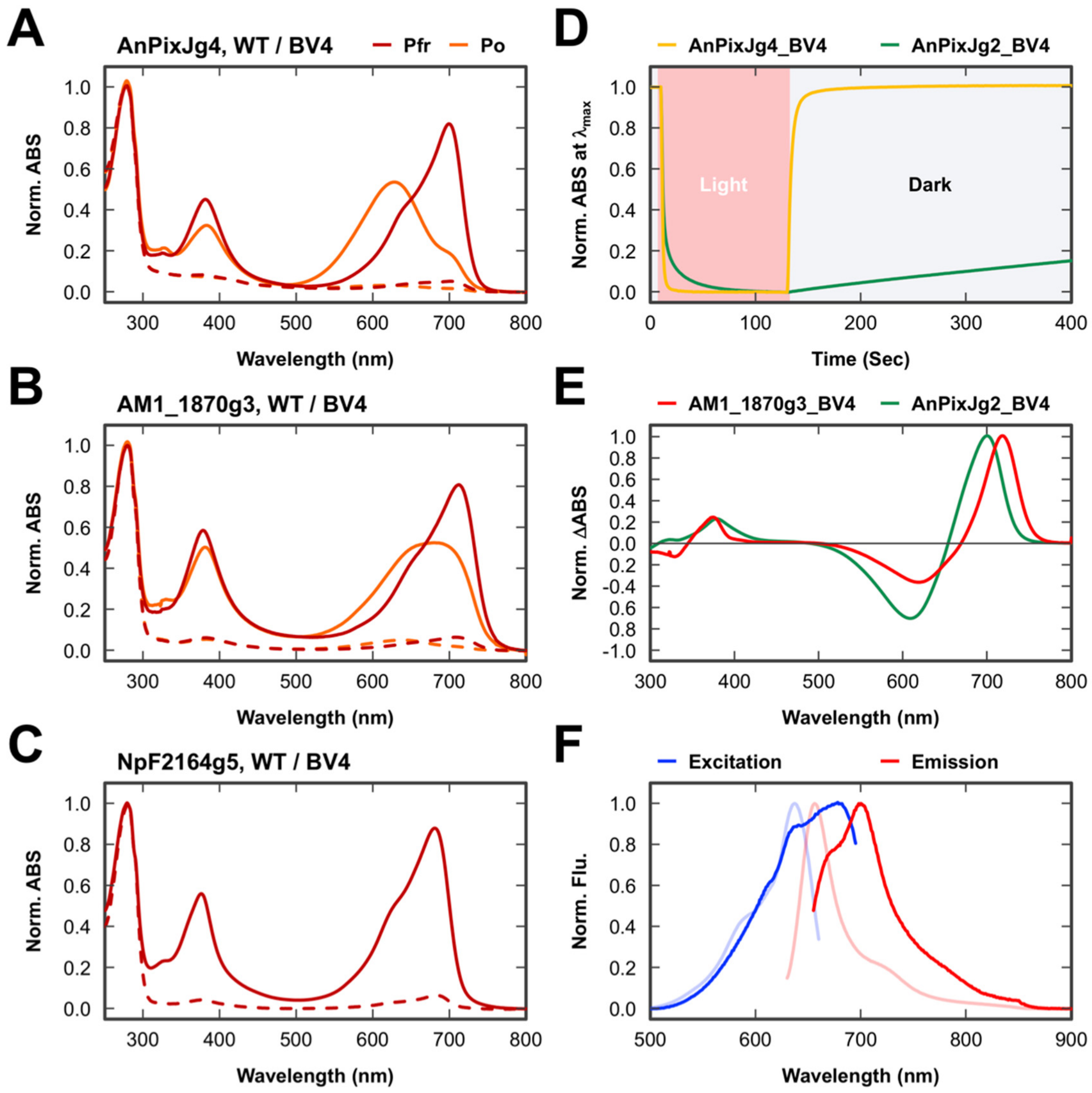
A
AnPixJg4, WT / BV4
Pfr
Po
Norm. ABS
1.0
0.8
0.6
0.4
0.2
0.0
300
400
500
600
700
800
Wavelength (nm)
B
AM1_1870g3, WT / BV4
Norm. ABS
Wavelength (nm)
C
NpF2164g5, WT / BV4
Norm. ABS
Wavelength (nm)
D
AnPixJg4_BV4
AnPixJg2_BV4
Norm. ABS at λ_{max}
Light
Dark
0
100
200
300
400
Time (Sec)
E
AM1_1870g3_BV4
AnPixJg2_BV4
Norm. ΔABS
1.0
0.8
0.6
0.4
0.2
0.0
0.2
-0.4
0.6
0.8
-1.0
Wavelength (nm)
F
Excitation
Emission
Norm. Flu.
500
600
700
800
900
Wavelength (nm)

Fig. 4

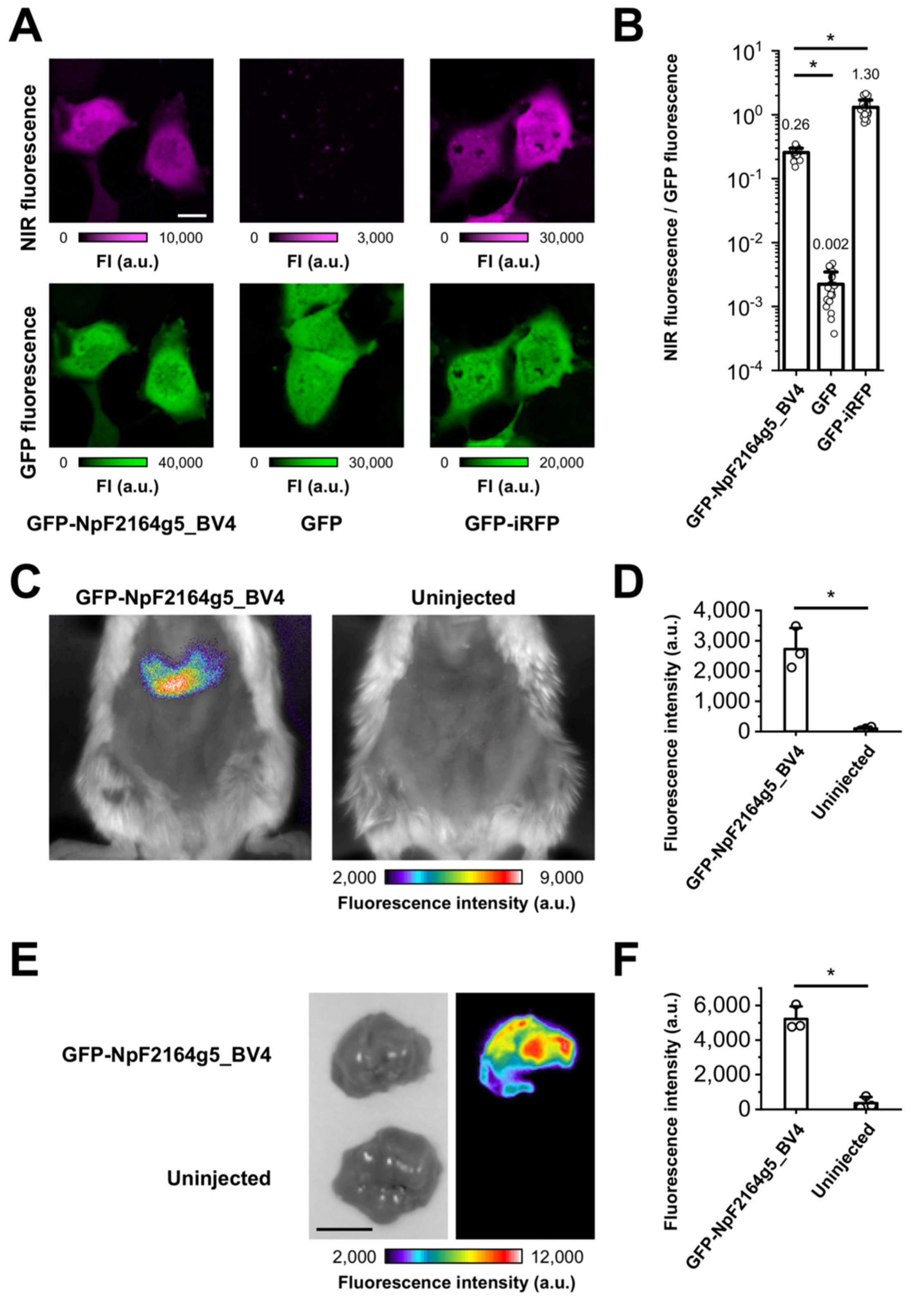
A
NIR fluorescence
GFP fluorescence
0
10,000
3,000
30,000
40,000
20,000
FI (a.u.)
GFP-NpF2164g5_BV4
GFP
GFP-iRFP
B
NIR fluorescence / GFP fluorescence
10^1
10^0
10^{-1}
10^{-2}
10^{-3}
10^{-4}
0.26
0.002
1.30
*
C
Uninjected
2,000
9,000
Fluorescence intensity (a.u.)
D
4,000
3,000
2,000
1,000
0
E
F
6,000
12,000